



Mantle flow beneath northwestern Venezuela: Seismic evidence for a deep origin of the Mérida Andes

Jeniffer Masy^{a,*}, Fenglin Niu^a, Alan Levander^a, Michael Schmitz^b

^a Department of Earth Science, Rice University, Houston, TX, USA

^b Fundación de Investigaciones Simológicas (FUNVISIS), Caracas, Venezuela

ARTICLE INFO

Article history:

Received 10 December 2010
Received in revised form 10 March 2011
Accepted 15 March 2011
Available online 8 April 2011

Editor: P. Shearer

Keywords:

Mérida Andes
seismic anisotropy
vertical coherent deformation
trench-parallel mantle flow

ABSTRACT

We measured shear wave splitting from SKS data recorded by the national seismic network of Venezuela and a linear broadband PASSCAL/Rice seismic array across the Mérida Andes. The linear array was installed in the second phase of the passive seismic component of the BOLIVAR project to better understand the complicated regional tectonics in western Venezuela. Using the method proposed by Wolfe and Silver (1998), SKS waveforms from 2 to 36 earthquakes, mostly from the Tonga subduction zone, were selected for each of the 23 stations in the region in order to do splitting analysis. The fast polarization directions can be divided into 3 zones, all in agreement with local GPS data: The first zone comprises the stations north of the dextral strike-slip Oca–Ancon fault. These stations show the largest split times (1.6–3.2 s), oriented in a roughly EW direction, and are similar to splitting observations made further to the east along the strike slip plate boundary (Growdon et al., 2009). We attribute this to trench-parallel mantle flow that passes around the northwest corner of the subducting Caribbean plate and along the northern edge of South America as proposed by Russo and Silver (1994), forming an eastward flow beneath the southern Caribbean plate. Zone two is the Mérida Andes, with the right lateral Bocono fault in the center, where split orientations are at ~N45°E, suggesting that the observed seismic anisotropy is likely caused by lithospheric deformation parallel to the Bocono fault. Zone three is east of the Bocono fault inside the Barinas–Apure Basin, where the measured split times are smaller (~0.8 s) with an EW fast direction that is consistent with those observed at the Guarico Basin, Maturin Basin and the Guayana Shield in the east, and are interpreted as orientation with the motion of the continent.

© 2011 Elsevier B.V. All rights reserved.

1. Introduction

The boundary between the Caribbean (CAR) and South American (SA) plates in western Venezuela is a wide area where active faults and extensive deformation are observed (e.g. Audemard and Audemard, 2002; De Toni and Kellogg, 1993). Transpressional faulting has divided the boundary region into several distinct tectonic blocks that move independently of the surrounding plates. For example, the triangular Maracaibo Block (MB), bounded by the left-lateral strike-slip Santa Marta–Bucaramanga (SMB) Fault to the southwest, by the right-lateral strike-slip Bocono Fault to the southeast, and by the right-lateral strike-slip Oca–Ancon (OA) Fault to the north, is moving northeastward relative to the SA plate as if it is escaping from the continent (Fig. 1). Intracontinental deformation within northern Colombia and northwestern Venezuela is revealed by the presence of the northern end of the Andean belt, known as the Eastern Cordillera. The Cordillera consists of three recently uplifted (<10 Myr) mountain chains: the Mérida Andes in Venezuela, the Perija Range,

straddling the Venezuelan–Colombian border, and the Santa Marta block in Colombia (e.g., Audemard and Audemard, 2002; Kellogg and Bonini, 1982). Although it is generally believed that timing of the uplift is related to the late Miocene–Pliocene collision of the Panama arc with the South America (Molnar and Sykes, 1969), the uplift is likely the result of flat slab subduction of the southern edge of CAR under northern South America (Bezada et al., 2010; Kellogg and Bonini, 1982).

GPS measurements clearly indicate oblique convergence between the western part of the CAR and the SA plate (Fig. 1, Weber et al., 2001). Tomographic studies suggest the CAR plate starts to subduct beneath SA at offshore of the Santa Marta Massif with a very low angle (Malave and Suarez, 1995; Taboada et al., 2000; Van der Hilst and Mann, 1994). It then dips steeply to the ESE under the Mérida Andes (Bezada et al., 2010; Taboada et al., 2000). This subduction is likely responsible for the uplift and deformation observed in the region. Beside the three major uplifts, moderate deformation and seismicity are observed in the Serrania de Falcon located in the northeastern Maracaibo block, as well as under the central Maracaibo block. Several models have been proposed to explain the observed formations, and most invoke shallow processes (for example type A, continent–continent, subduction) for the orogeny (e.g., Audemard and Audemard, 2002; Kellogg and Bonini,

* Corresponding author. Tel.: +1 713 348 3048; fax: +1 713 348 5214.
E-mail address: jm15@rice.edu (J. Masy).

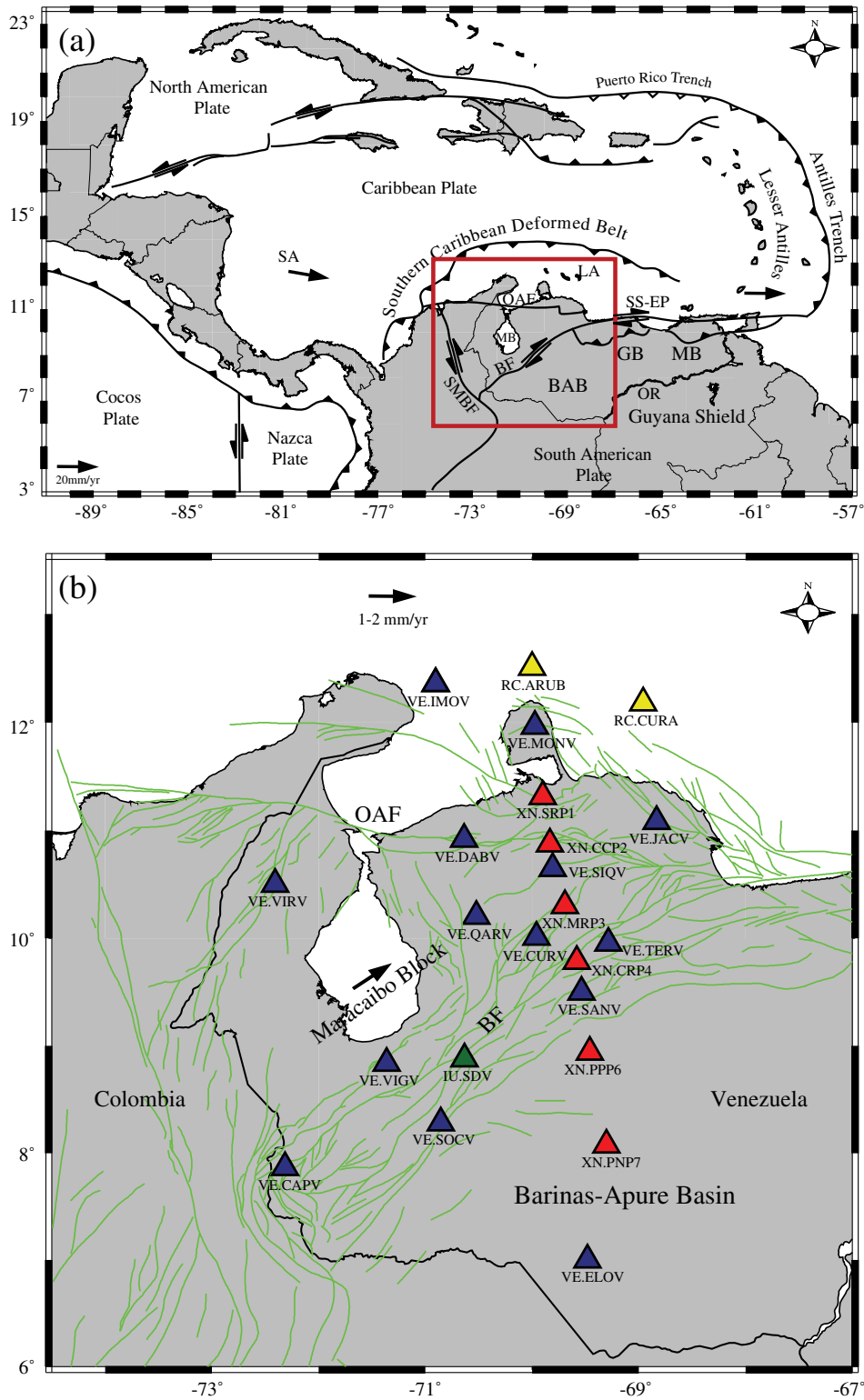


Fig. 1. (a) Caribbean tectonics, with GPS vectors in the southern Lesser Antilles Arc and on San Andreas (SA) Island in the western Caribbean. Red box indicates the study region shown in (b). (b) Broadband seismic stations (with Seismic code) in western Venezuela used in the investigation of upper mantle anisotropy and deformation. Blue triangles indicate permanent stations of the National Seismic Network of Venezuela. Yellow and red triangles represent temporal deployments under the first and second phases of the BOLIVAR project. Light green are active faults. MB: Maracaibo Block, BF: Bocono Fault, OAF: Oca–Ancon Fault; SMBF: Santa Marta–Bucaramanga Fault; SS–EP: San Sebastian–El Pilar Fault BAB: Barinas–Apure Basin; GB: Guarico Basin; MB: Maturin Basin; OR: Orinoco River.; and LA: Leeward Antilles. (For interpretation of the references to color in this figure legend, the reader is referred to the web version of this article.)

1982). Thus far, there is little data, especially deep seismic data, with which to evaluate these models.

Seismic anisotropy provides essential information about the style and geometry of mantle deformation. Seismic waves in an anisotropic

media travel with different speeds depending on their propagation and polarization directions. The major upper mantle mineral, olivine, has a highly anisotropic crystal structure, with up to 25% variation in P- and S-wave velocities. These anisotropic minerals can be aligned

preferentially through mantle deformation, resulting in seismic anisotropy with a reduced magnitude of a few percent (e.g. Silver, 1996). In areas where lithosphere is undergoing shortening, the fast directions tend to parallel to the strike of the orogenic belts. Meanwhile, seismic anisotropy also seems to have a close correspondence to horizontal mantle flow developed under a simple shear setting beneath the station (e.g., Silver, 1996). The close relationship between the stress/strain field and seismic anisotropy thus can be used to map upper-mantle deformation associated with a wide range of tectonic processes.

Measuring shear wave splitting, or birefringence is one of the most effective methods to characterize seismic anisotropy in the upper mantle (e.g., Savage, 1999; Silver, 1996). The polarization direction of the fast shear wave, φ , and the delay time between the fast and slow waves, δt , are used to parameterize seismic anisotropy. Russo et al. (1996) found that stations located at the southeastern CAR–SA plate boundary exhibit a nearly east–west fast direction with unusually large splitting times of ~ 2 s. This is approximately twice as large as the global average of ~ 1 s (Silver, 1996). Growdon et al. (2009) measured waveform splitting of the core phases, SKS/SKKS, recorded by the broadband seismic stations deployed under the BOLIVAR (Broadband Onshore–Offshore Lithospheric Investigation of Venezuela and the Antilles Arc Region), and obtained very large splitting times from stations deployed at the northeastern coast of Venezuela, consistent with the results of Russo et al. (1996). They also found that the splitting time drops quickly towards the interior of the SA. Most of the stations located at the Guayana shield, Maturin basin show a splitting time < 1 s. They interpreted the large splitting times observed in northeastern Venezuela as caused by a strong mantle flow associated with a slab tear. The Atlantic slab is tearing from continental South America in response to the eastward retreat of the Antilles trench. In addition to the SKS splitting data, the tear was also suggested by a variety of seismic data, such as local seismicity and active source reflection/refraction data (Clark et al., 2008a,b), surface wave (Miller et al., 2009), body wave tomography (Bezada et al., 2010), and receiver function data (Huang et al., 2010; Niu et al., 2007), and seems to play a major, if not dominant, role in the regional tectonics.

Most of the broadband seismic stations were installed in eastern Venezuela during the main phase deployment of the BOLIVAR project, leaving it difficult to address important tectonic issues along the CAR–SA plate boundary in northwestern Venezuela, such as the slab geometry of the Caribbean plate subducted under northwestern SA, and its role in uplift of the Mérida Andes, the Perija and Santa Marta mountain ranges, and development of the Maracaibo block generally. During the second phase of BOLIVAR, we installed a linear broadband array across the northeastern end of the Mérida Andes. In this paper we present a summary of seismic anisotropic structure beneath western Venezuela estimated from data recorded by the linear array as well as by the National Seismic Network of Venezuela. Our goal is to characterize the relationships between plate motions, and the style of crustal and mantle deformation for the study region. Results are consistent with previous studies but also provide new constraints on mantle deformation along the mountain belts.

2. Data and analysis

We used SKS/SKKS waveform data recorded at 23 broadband seismic stations deployed in western Venezuela (Fig. 1b). 14 stations belong to the permanent National Seismic Network of Venezuela operated by the Fundación Venezolana de Investigaciones Sismológicas (FUNVISIS). We installed 2 Rice stations on the islands Curacao and Aruba during the first phase of the BOLIVAR deployment and we had two- and five-years of data from these two stations, respectively. The linear seismic array across the Mérida Andes consisted of 6 broadband stations that operated from October 2008 to November 2009. We also analyzed data recorded by the GSN (Global Seismic Network) station SDV from earthquakes occurring between 1994 and 2000.

We manually checked all the SKS/SKKS data recorded at epicentral distances between 85° and 120° from earthquakes with a magnitude > 5.6 , and selected 253 SKS/SKKS seismograms with good signal-to-noise ratio (SNR). No good data were acquired by station MRP3, but the other 22 stations have at least three good SKS/SKKS records (Table 1). A total of 122 events were used, among which 57 were recorded by the GSN station SDV. The remaining 65 events occurred between December 2003 and August 2009. Most of the earthquakes are from the southwest Pacific, the northwest Pacific, and the Mediterranean Sea regions, clustering into three back azimuthal directions that are roughly perpendicular or parallel to each other (Fig. 2). The FUNVISIS and Rice stations were recorded with a sampling rate of 100 samples per second (sps). They were decimated to 40 sps to be consistent with the sampling rate of the BOLIVAR linear array stations. We further filtered the data with a bandpass filter of 0.05–0.5 Hz before measuring the fast direction and splitting time.

To better constrain the splitting parameters (φ , δt), we have applied a multiple event stacking approach similar to the one developed by Wolfe and Silver (1998). Instead of estimating individual (φ , δt) sequentially for multiple earthquakes, the multi-event stacking method solves a pair of φ and δt that minimizes either the summed energy in the transverse component

$$E_T(\varphi, \delta t) = \left(\sum_{i=1}^N w_i E_{Ti}(\varphi, \delta t) \right) / \sum_{i=1}^N w_i, \quad (1)$$

or the summed second eigenvalue λ_2 of the covariance matrix of the corrected particle motion (Li and Niu, 2010)

$$\Lambda_2(\varphi, \delta t) = \left(\sum_{i=1}^N w_i \lambda_{2i}(\varphi, \delta t) \right) / \sum_{i=1}^N w_i. \quad (2)$$

here $E_{Ti}(\varphi, \delta t)$ and $\lambda_{2i}(\varphi, \delta t)$ are, respectively, the transverse energy and the smaller eigenvalue of the covariance matrix of the i th event, computed after correcting wave propagation effects in an anisotropic medium with a fast polarization direction of φ and delay time of δt . w_i is the weight of the i th event and is taken as the averaged signal-to-noise (SNR) of the two horizontal components, and N is the total number of the events. To compute the SNR, we chose a noise time window before the SKS arrival with the same length as the SKS signal. We also used the total SKS energy recorded at the two horizontal

Table 1
SKS splitting parameters.

Station	Lon. ($^\circ$)	Lat. ($^\circ$)	# of events	# of azimuth	φ ($^\circ$)	δt (s)
ARUB	−70.001	12.509	3	2	84 ± 9	2.0 ± 0.3
IMOV	−70.902	12.358	3	2	82 ± 5	1.9 ± 0.3
CURA	−68.959	12.180	6	4	90 ± 10	2.1 ± 0.3
MONV	−69.970	11.955	3	1	73 ± 4	2.0 ± 0.7
SRP1	−69.900	11.318	4	2	90 ± 12	1.7 ± 0.3
JACV	−68.830	11.087	5	3	80 ± 6	2.1 ± 0.5
DABV	−70.636	10.922	20	3	84 ± 7	1.3 ± 0.3
CCP2	−69.833	10.879	8	2	87 ± 5	3.2 ± 0.7
SIQV	−69.808	10.649	24	3	76 ± 4	2.0 ± 0.3
VIRV	−72.406	10.503	22	3	52 ± 8	0.5 ± 0.1
QARV	−70.524	10.207	7	2	78 ± 3	0.5 ± 0.2
CURV	−69.961	10.013	7	2	75 ± 14	1.0 ± 1.0
TERV	−69.192	9.964	13	4	32 ± 7	1.1 ± 0.3
CRP4	−69.583	9.788	10	4	50 ± 5	1.3 ± 0.4
SANV	−69.536	9.501	10	4	54 ± 7	1.0 ± 0.4
PPP6	−69.460	8.941	5	4	71 ± 10	0.7 ± 0.4
SDV	−70.633	8.879	57	3	54 ± 5	1.2 ± 0.4
VIGV	−71.364	8.840	11	2	65 ± 6	1.3 ± 0.4
SOCV	−70.857	8.284	8	3	55 ± 5	1.4 ± 0.3
PNP7	−69.302	8.074	3	1	85 ± 8	1.0 ± 0.4
CAPV	−72.314	7.865	13	2	43 ± 9	0.8 ± 0.2
ELOV	−69.483	7.001	11	3	76 ± 8	0.7 ± 0.3

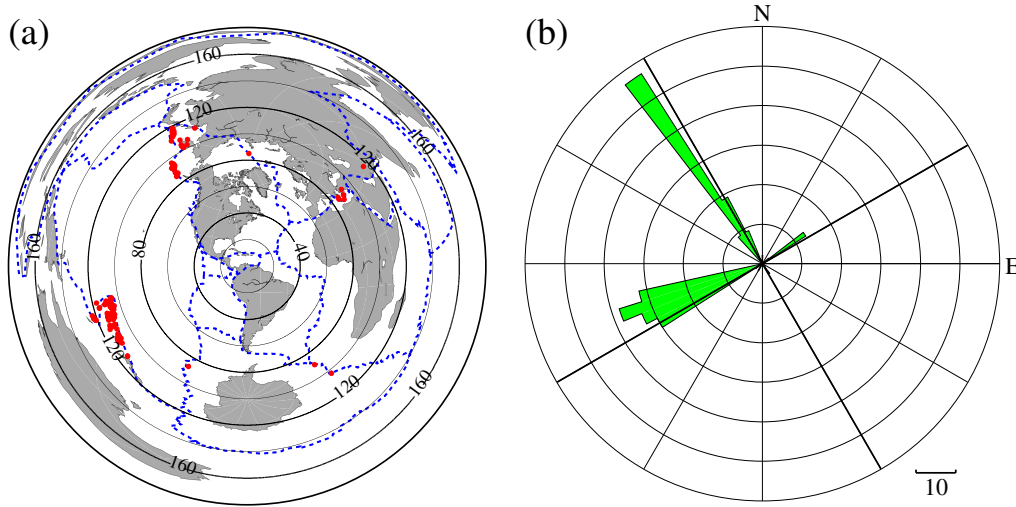


Fig. 2. (a) Locations (red dots) of the 122 events located at 85°–120° distance from the 22 stations used in this study. Note most of earthquakes occurred in the Tonga subduction (SW), the Japan–Kurile–Kamchatka–Aleutian Arcs (NE), and the Mediterranean region (NE). Only three earthquakes are from the Mid-Atlantic Ridge and one from the East Pacific Rise (SSE and SSW, respectively). At (b) Back azimuthal distribution of the 122 events, showing the number of events in each 5-degree bin. Note that the source regions have back azimuths approximately 90° apart, making it difficult to use them to investigate azimuthal dependence of the splitting parameters. (For interpretation of the references to color in this figure legend, the reader is referred to the web version of this article.)

components to normalize the traces before computing the transverse energy $E_T(\varphi, \delta t)$ in order to ensure each event has the same contribution to the total energy. We varied φ in the range of 0° to 180° with an increment of 1°, and δt from 1.0 to 4.0 s in increments of 0.05 s. With the measured $(\varphi, \delta t)$, we further computed the polarization directions of the SKS arrivals to make sure that they are consistent with the geometric back azimuths. Differences between the calculated polarization directions and geometric back azimuths usually vary from -15° to 15° with a mean close to zero. Since the calculated polarization could be affected by sensor misorientation, we further used the particle motions of the direct P waves to calibrate the sensor orientations (Niu and Li, 2011). We found that all the stations used in this study were properly aligned with an error $<10^\circ$.

We also used the method of Li and Niu (2010) to compute errors in measuring the splitting parameters $(\varphi, \delta t)$:

$$\frac{E_T(\varphi, \delta t)}{E_T^{noise}} \leq 1 + \frac{k}{n-k} f_{k, n-k}(1-\alpha). \quad (3)$$

here n is the number of degrees of freedom, which was calculated based on the method of Silver and Chan (1991). α is the confidence level, $k=2$ is the number of parameters, and f represents the F-distribution. E_T^{noise} is the noise energy and was calculated by averaging the noise levels of the two horizontal components.

In general, the joint solution determined from the summed transverse energy agrees with individual solutions of each event and falls into a narrowly defined region into the $(\varphi, \delta t)$ domain (Fig. 3a–i). This can be further demonstrated by overlapping individual solutions on the $(\varphi, \delta t)$ plane. For each event, we assigned a unit value to a grid if the grid is situated in the solution region (red area in Fig. 3a–h) defined by (3). Zero value is given otherwise. That is

$$n_i(\varphi, \delta t) = \begin{cases} 1, & \text{if } (\varphi, \delta t) \text{ falls in the 95\% confidence region} \\ 0, & \text{otherwise} \end{cases} \quad (4)$$

these individual solution regions were then overlaid and grid values were averaged:

$$n(\varphi, \delta t) = \frac{1}{N} \sum_{i=1}^N n_i(\varphi, \delta t) \quad (5)$$

The grids with an average value of one (red area in Fig. 3j) were considered to be possible solutions and we took the average $(\varphi, \delta t)$ as the final solution. In general the optimum $(\varphi, \delta t)$ estimated from the two methods agree with each other, but the overlapping method yields a more tightened solution region (Fig. 3j) than that constrained by the multi-event stacking method (Fig. 3i).

3. Results and discussion

We applied the above stacking method to all the 22 stations that have high SNR SKS/SKKS data. To ensure our measurements robust, we used the following criteria in the splitting analysis: (1) energy on the transverse component is significantly reduced after the correction of anisotropy, (2) difference in the fast-axis direction measured from minimizing transverse energy and second eigenvalue is small (within the error), and (3) the measurements are not affected by the selection of time window length. Among the 22 stations, CCP2 had the largest splitting time, 3.2 ± 1.0 s, in the region (Fig. 3i and j). This unusual large splitting time is consistent with single-event based measurements (Fig. 3a–h), and is nearly insensitive to the selection of SKS/SKKS time windows. Fig. 4a shows the uncorrected eight SKS/SKKS waveforms recorded at the station. The SKS/SKKS phase is clearly shown in the transverse component with amplitudes comparable to the radial ones (Fig. 4a). Most of them exhibited an elliptical particle motion (Fig. 4b). After the correction of seismic anisotropy, the transverse component shows virtually no SKS/SKKS energy (Fig. 4c), and their particle motions are almost linear (Fig. 4d). Silver and Chan (1988) showed that the radial and transverse components $u_R(t)$ and $u_T(t)$ are related to the source waveform $s(t)$ by the following two equations:

$$\begin{aligned} u_R(t) &= s(t) \cos^2 \phi + s(t-\delta t) \sin^2 \phi \\ u_T(t) &= [s(t) - s(t-\delta t)] \sin \phi \cos \phi \end{aligned} \quad (6)$$

here ϕ is the angle between the fast and radial directions. When δt is small compared to the dominant period of $s(t)$, the transverse component, $u_T(t)$, is approximately proportional to the time derivative of the radial component, $u_R(t)$. The uncorrected seismograms in Fig. 4a clearly show this feature.

The estimated splitting parameters $(\varphi, \delta t)$ for each station are listed in Table 1 and are shown in Fig. 5. Uncertainties in φ and δt were

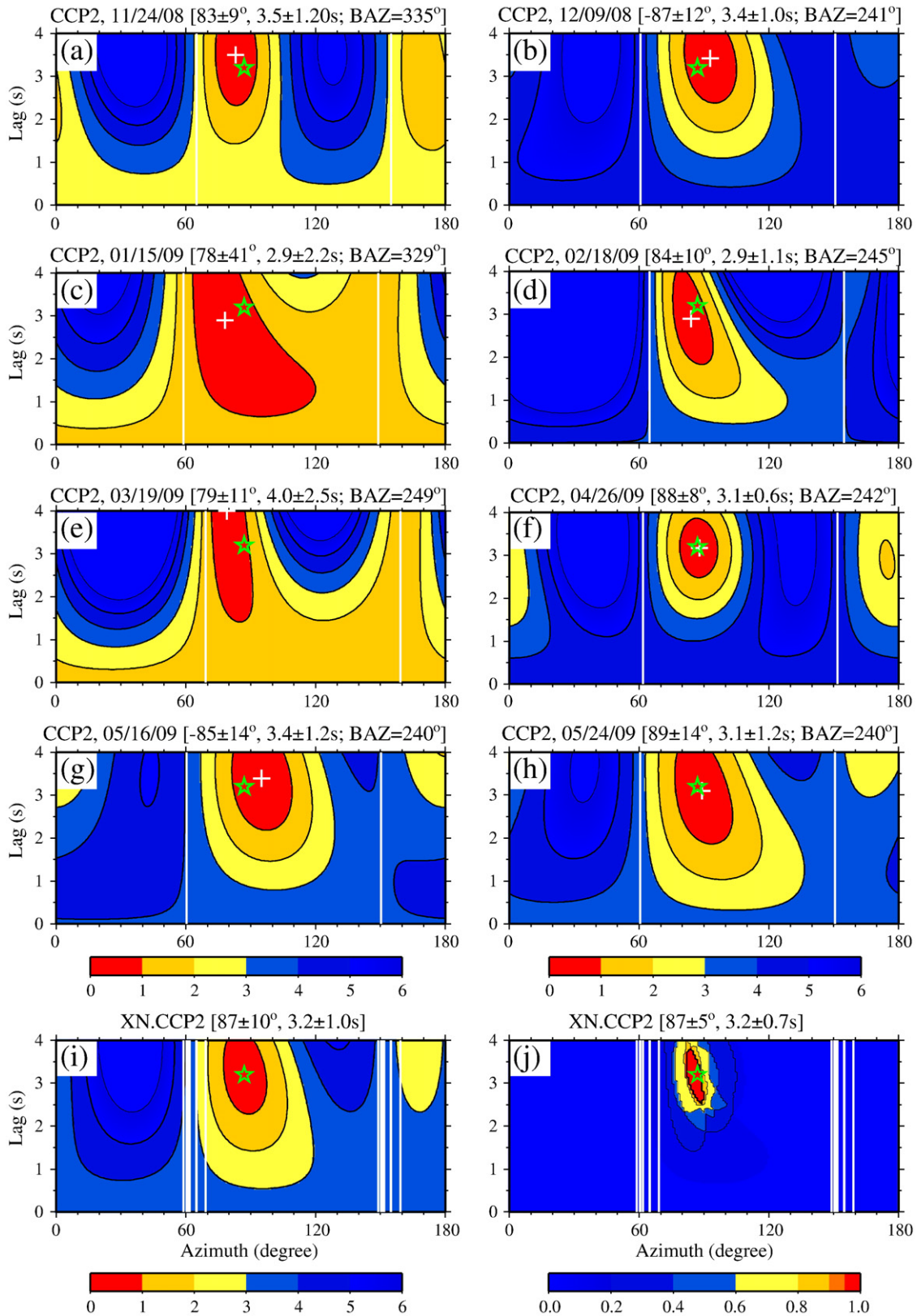


Fig. 3. Estimates of the two splitting parameters ($\varphi, \delta t$). (a–h) Color contour plot of $E_T(\varphi, \delta t)$ for the 8 events used in estimating the optimum ($\varphi, \delta t$). White plus and red area represent the minimum value and the 95% confidence region, respectively. Green star indicates the joint solution of the events. The two vertical lines indicate the polarization direction of the incoming SKS/SKKS wave and its perpendicular direction. Color scales used in plotting the contours are shown below the plots. (i) Color contour plot of summed transverse energy $E_T(\varphi, \delta t)$. Green star and red area indicate the minimum value and the 95% confidence region. Vertical white lines indicate the back azimuths of the 8 events and their perpendicular directions. (j) Color contour plot of averaged grid count $n(\varphi, \delta t)$ defined by Eq. (5). Red area indicates 95% confidence region constrained by all the events. Green star is the average of 95% confidence region. (For interpretation of the references to color in this figure legend, the reader is referred to the web version of this article.)

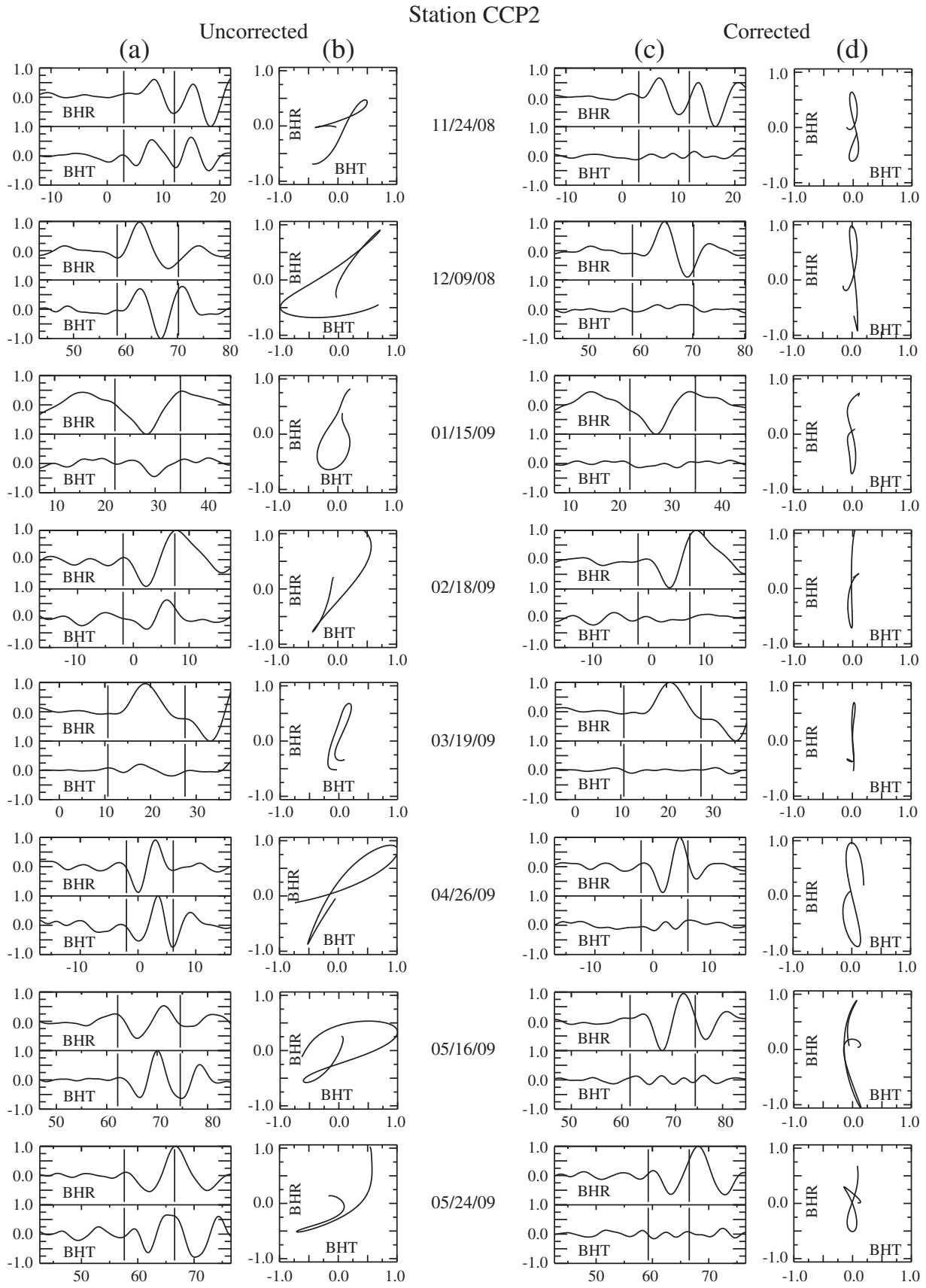


Fig. 4. (a) Original radial and transverse components of the 8 events. Their corresponding splitting measurements are shown in Fig. 3. Note the large SKS/SKKS amplitude in the transverse component. (b) Particle motion of the radial and transverse components. (c) Corrected radial and transverse components. Note that in the corrected seismogram, the transverse component shows little or no SKS/SKKS energy. (d) Particle motion of the corrected radial and transverse components, note the change from an elliptical to linear particle motions.

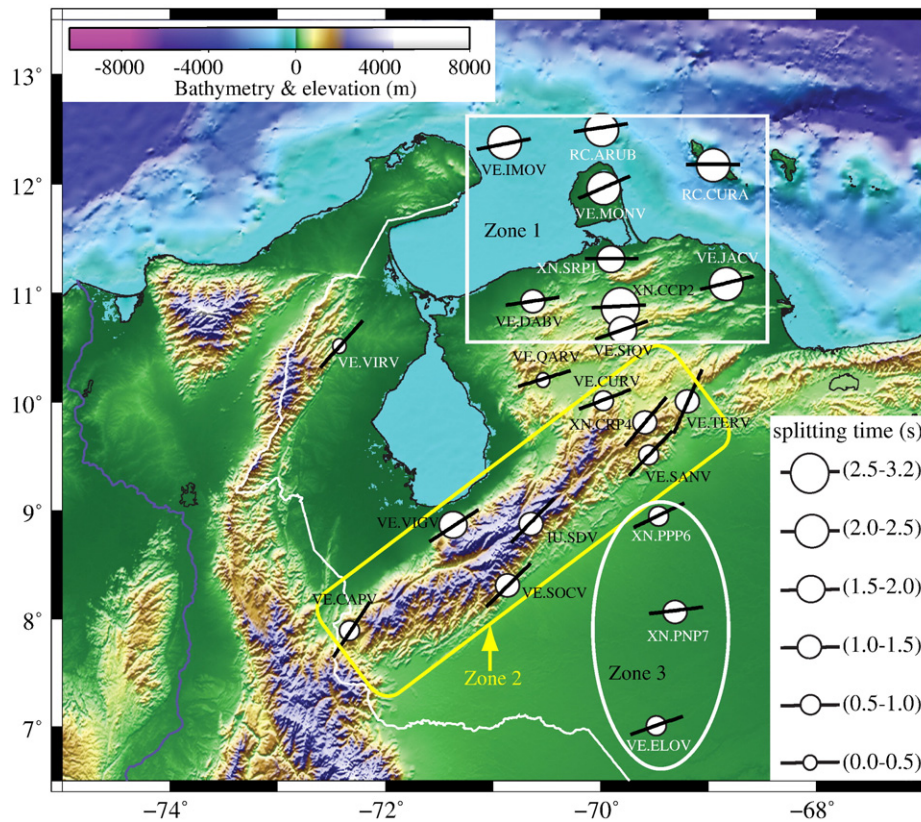


Fig. 5. Measured splitting parameters are shown together with the topography of the study region. The orientation of the black solid lines indicates the orientation of the fast direction. In general the study area can be divided in 3 different zones. The first one is north of the Oca–Ancon dextral strike slip fault, where splitting times are the largest (1.6–3.2 s) with an east–west orientation. The second zone, southeast of the Maracaibo Block, shows a splitting direction N45E, parallel to Bocono Fault and Mérida Andes. In the third zone (inside Barinas–Apure Basin) also with an east–west orientation, the smallest delay times are observed (~0.8 s). (For interpretation of the references to color in this figure legend, the reader is referred to the web version of this article.)

estimated by the overlapping method. We also listed the numbers of events and back azimuths used in the measurements. Among the 22 stations measured, 20 have events arriving from at least two back azimuthal directions (Table 1, Fig. 2). For all the 22 stations, we were able to find a common solution that falls into the individual solution regions of all the events. For a homogenous anisotropic layer with a horizontal symmetry axis, φ and δt measured from waves arriving from different azimuths are expected to have the same values. When a dipping symmetry axis or a depth varying anisotropy is present (e.g., Schulte-Pelkum and Blackman, 2003; Silver and Savage, 1994), φ and δt would show a periodic azimuthal variation with a period of 90° . As mentioned above, most of the stations have only 2 to 3 back azimuths that are approximately 90° apart (Fig. 2b). The poor distribution in azimuth of the data here does not allow us to examine depth variation of the anisotropic structure beneath the study region. Our interpretation will be focused on the large lateral variations seen in the area.

We have 9 stations located at three islands and along the coast north to the now largely inactive dextral strike–slip Oca–Ancon fault (white box in Fig. 5). All the stations show a fast direction roughly parallel to the EW direction. The splitting times vary from 1.3 s to 3.2 s with an average of 2.0 s, which is consistent with the large delay times observed from stations deployed along the eastern section of the CAR–SA plate boundary adjacent to the active plate boundary strike–slip faults (Crowdon et al., 2009; Russo et al., 1996). As mentioned above, we paid special attention to consistency between different events in determining the splitting parameters; it is unlikely that the large delay times observed here are caused by contamination from some particular ray paths. Also, measured splitting parameters for raypaths originating in Tonga and in the Japan–Kurile–Kamchatka–Aleutian regions were similar, implying that the splitting is accumu-

lated along the upper mantle part of the raypath beneath the station. In principle, either a thick or a strong anisotropic layer can result in a large delay time. For example, a 5% S-wave anisotropy is sufficient to give a delay time of 2 s in a 200-km thick upper-mantle layer. Thus to explain the largest 3.2 s delay time observed here, an S-wave anisotropy of 7–8% is required if we fixed the anisotropic thickness to the ~200 km. Mainprice and Silver (1993) calculated S-wave anisotropy of natural xenolith and ophiolite samples and found that the ophiolite samples are twice as anisotropic (maximum anisotropy of 8–9%) as the kimberlite nodules (maximum anisotropy of ~3.7%). Thus it is still possible to produce a ~2–3 s delay time within a boundary where subduction of oceanic lithosphere is involved.

Russo and Silver (1994) proposed a large-scale trench-parallel mantle flow beneath the Nazca slab based on a compilation of seismic anisotropy measurements made along the west coast of South America. Although the Nazca plate is subducting beneath the SA plate, the Nazca trench is retreating progressively to the west. The combination of the two motions is known as retrograde motion. If the slab is decoupled from the mantle below, the retrograde motion of the slab exerts stress on the asthenosphere beneath it, leading to the development of a trench-parallel flow below the slab. Based on subduction geometry, Russo and Silver (1994) further hypothesized that the flow is initiated at the coast of the central Andes and moves north and south separately along the coast. Both branches of the flow are diverted eastward when they clear the edge of the subducting plates beneath the Caribbean and Scotia Sea. The eastward flow beneath the CAR, coupled with the eastward translation of the Atlantic slab created a strong vertically coherent shear along the strike–slip El Pilar fault systems between the southeastern CAR and the SA plates. Crowdon et al. (2009) and Russo et al. (1996) attributed

the observed large splitting times to a vertical shear directly beneath the plate boundary. [Growdon et al. \(2009\)](#) also found that the estimated delay times decrease quickly toward south in eastern Venezuela, indicating that the flow induced strain must drop rapidly away from the boundary.

We also consider the large splitting time observed in the western coast of Venezuela to be associated with the large-scale retrograde flow proposed by [Russo and Silver \(1994\)](#) ([Fig. 6](#)). As mentioned before, tomography images ([Bezada et al., 2010; Van der Hilst and Mann, 1994](#)) showed that the southern edge of the CAR plate is subducting beneath the Santa Marta and Perija ranges along a WNW–ESE direction. The P-wave tomography images of [Bezada et al. \(2010\)](#) showed that the Caribbean plate starts subduction beneath northern Colombia at a very low angle and then dips almost vertically beneath the eastern flank of the Perija Range and Lake Maracaibo. A slab tear was hypothesized to separate the steeply dipping slab from the Caribbean to the north ([Taboada et al., 2000](#)) ([Fig. 6](#)). We speculated that the retrograde flow passes around the northwestern corner of the SA plate at a location far west to the subducting Caribbean slab, as we observed minor seismic anisotropy (0.0–0.5 s) at VIRV located at the east flank of the Perija Range. The subducting slab thus may act like a barrier that prevents the retrograde flow from entering below the SA plate and directs the flow toward the northern edge of the slab below the hypothesized tear. To produce the observed 2 to 3 s delay time, the flow has to have a vertical dimension of ~200 km if we assume S-wave anisotropy of 8%.

The 3 stations inside the Barinas–Apure basin situated at the southeast side of the Bocono Fault (white ellipse in [Fig. 5](#)) recorded the lowest splitting times, ~0.8 s among all the stations (except for VIRV and QARV, [Table 1](#)). The estimated fast directions average to 77° or 257° East of North, consistent with the absolute motion (~262° clockwise from north) of the SA plate ([Gripp and Gordon, 2002](#)). The estimated fast directions and delay times are also consistent with those observed in the Maturin basin and the Guayana shield in eastern Venezuela ([Growdon et al., 2009](#)). We thus interpret the observed seismic anisotropy to be caused by a simple asthenospheric flow parallel to plate motion.

While stations along the coast and within the Barinas–Apure basin exhibited an ~EW fast direction, the 8 stations in the Mérida Andes

(yellow rectangle in [Fig. 5](#)) showed an NE–SW fast direction, parallel to the strike of the Mérida Andes. Moderate delay times were obtained from these stations with amplitude varying from 1 to 1.4 s. [Pinero-Feliciangeli and Kendall \(2008\)](#) measured ($\varphi, \delta t$) at the GSN station SDV and found similar alignment between the fast polarization direction and geological strike. As described above, seismic anisotropy measured from SKS waveform splitting is closely related to the deformation style and geometry in the upper mantle. Thus the good coherence between the geologic fabric and the fast direction observed here suggests that the crust and the upper mantle of the Mérida Andes deform coherently ([Fig. 6](#)) in response to compressional forces related to uplift of the mountains. Assuming a maximum S-wave anisotropy of 4% ([Mainprice and Silver, 1993](#)), we estimated that the deformed subcontinental mantle extends to a depth of ~150–200 km in order to generate a 1–1.4 s splitting time if we assume anisotropy is evenly distributed across the lithosphere.

Deformation associated with the uplift of the Mérida Andes has been assumed to be confined within the crust and to be related to type-A (continent–continent) subduction, although it is still debated on whether the subduction is SE- (e.g., [Burke, 1988; Colletta et al., 1997; Kellogg and Bonini, 1982](#)) or NW-directed (e.g., [Audemard and Audemard, 2002](#)). Our measurements of splitting times here, however, suggest that beneath the mountain range a vertically coherent deformation extends much deeper than the crust–mantle boundary, which is estimated to be ~50 km deep ([Niu et al., 2007](#)). This is because: 1) if the thick crust is the main cause of the observed 1–1.4 s splitting time, then an unreasonably high crustal anisotropy (~10%) is required, as for a 50 km thick crust with an average S-wave velocity of 3.5 km/s, the travel time is approximately 14 s for a vertically propagating wave; 2) [Niu et al. \(2007\)](#) found that at the GSN station SDV the arrival time and amplitude of the Moho Ps conversion depend on the directions of the incoming P waves. The azimuthal variation, however, doesn't exhibit a π -periodicity, which is an indicator of crustal anisotropy. Rather, the variation can be better explained by a dipping Moho structure. Thus it is likely that the formation of the Mérida Andes has been accompanied by shortening of the entire lithosphere. As the surface deformation is highly localized in the Mérida Andes, we speculate that a weak and thin lithosphere may have been present under the mountain range before its recent uplift. There are geological and crustal seismic studies (e.g.,

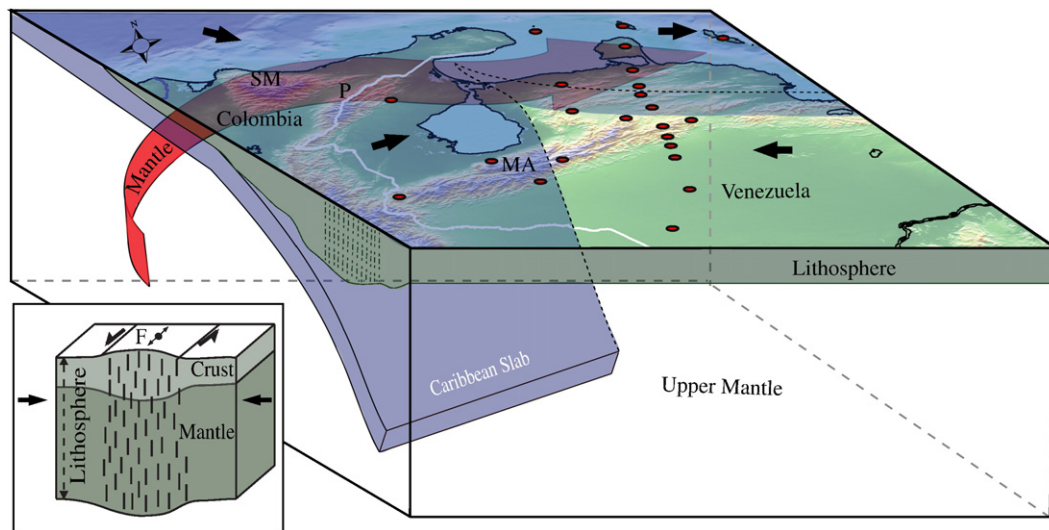


Fig. 6. Model of the subducting CAR plate with a hypothesized slab tear near the coast of western Venezuela that separates the subducting from the non-subducting Caribbean plate. Red arrow represents the large-scale mantle flow around the subducting plate, similar to that proposed by [Russo and Silver \(1994\)](#). The eastward flow produces a strong shear zone in the upper mantle along the CAR–SA plate boundary, which is observed as large splitting times in the coastal region adjacent to and north of the plate boundary. Along the Mérida Andes the split measurements suggest the entire lithosphere is deformed coherently parallel to the Bocono Fault (see the inset cartoon, which was modified from [Silver \(1996\)](#)), where F indicates the strike of the main fault and the arrows represent the direction of the shear stress field across the fault. Inside the Barinas–Apure Basin delay times are small with a direction consistent with the absolute motion direction of the South American plate. (For interpretation of the references to color in this figure legend, the reader is referred to the web version of this article.)

Audemard and Audemard, 2002; Colletta et al., 1997; Duerto et al., 2006; Kellogg and Bonini, 1982; Molnar and Sykes, 1969) suggesting the occurrence of active rifting in the study area during the Jurassic. Rift related Jurassic grabens have been found in outcrops and have been identified in seismic sections across the Mérida Andes.

4. Conclusions

We measured shear wave splitting at 22 stations in northeastern Venezuela with a multi-event stacking method. With the limited data, we found no apparent azimuthal variation of the splitting parameters and employed a one-layer anisotropic model in interpreting the measurements. We found three distinct areas with different orientations and magnitudes, and inferred three different deformation mechanisms across western Venezuela: (1) Stations located on north of the Caribbean–South American plate boundary on islands and in the coastal area north to the Oca–Ancon fault have the largest splitting times, ~2–3 s, and a fast direction parallel to the EW CAR plate motion direction, which can be explained by a strong eastward flow confined at the CAR–SA plate boundary. (2) Seismic anisotropy estimated from stations located within the stable SA plate is weak, is parallel to SA plate motion, and has an origin likely in the asthenosphere. (3) Intermediate splitting times, ~1.0–1.5 s, and an ~NE–SW fast direction are observed at stations deployed in the Mérida Andes, suggesting that the deformation of the crust and subcontinental mantle contributes to the anisotropy. It is likely that the lithospheric mantle plays a major, and possibly dominant, role in the formation of the Mérida Andes.

Acknowledgments

We thank FUNVISIS for providing the data used in this study, and for all the support and assistance they gave us during the deployment of seismic stations: Arturo Pernia, Edgar Rodriguez, Herbert Rendon, Claudia Quinteros, Ricardo Lopez. We also thank the IRIS-PASSCAL program for providing instruments and technical support during this project. Comments from two anonymous reviewers significantly improved the quality of this paper. This research is supported by the NSF continental dynamics program under grant EAR-0607801.

References

Audemard, F.E., Audemard, F.A., 2002. Structure of the Mérida Andes, Venezuela: relations with the south structure of the Me America–Caribbean geodynamic interaction. *Tectonophysics* 345, 299–327.

Bezada, M.J., Levander, A., Schmandt, B., 2010. Subduction in the southern Caribbean: Images from finite-frequency P wave tomography. *J. Geophys. Res.* 115, B12333. doi:10.1029/2010JB007682.

Burke, K., 1988. Tectonic evolution of the Caribbean. *Annu. Rev. Earth Planet. Sci.* 16, 201–230.

Clark, S.A., Zelt, C.A., Levander, A., Magnani, M.B., 2008a. Characterizing the Caribbean–South American plate boundary at 64°W using wide-angle velocity modelling. *J. Geophys. Res.* 113. doi:10.1029/2007JB005329.

Clark, S.A., Sobiesiak, M., Zelt, C.A., Magnani, M.B., Miller, M.S., Bezada, M., Levander, A., 2008b. Identification and tectonic implications of a tear in the South American plate at the southern end of the Lesser Antilles. *Geochem. Geophys. Geosyst.* 9, Q11004. doi:10.1029/2008GC002084.

Colletta, B., Roure, F., De Toni, B., Loureiro, D., Passalacqua, H., Gou, Y., 1997. Tectonic inheritance, crustal architecture, and contrasting structural styles in the Venezuela Andes. *Tectonics* 16, 777–794.

De Toni, B., Kellogg, J., 1993. Seismic evidence for blind thrusting of the northwestern flank of the Venezuelan Andes. *Tectonics* 12 (6), 1393–1409.

Duerto, L., Escalona, A., Mann, P., 2006. Deep structure of the Mérida Andes and Sierra de Perijá mountain fronts, Maracaibo Basin, Venezuela. *AAPG Bull.* 90, 505–528. doi:10.1306/10080505033.

Gripp, A.E., Gordon, R.G., 2002. Young tracks of hotspots and current plate velocities. *Geophys. J. Int.* 150, 321–361.

Growdon, M.A., Pavlis, G.L., Niu, F., Vernon, F.L., Rendon, H., 2009. Constraints on mantle flow at the Caribbean–South American plate boundary inferred from shear wave splitting. *J. Geophys. Res.* 114, 1–7. doi:10.1029/2008JB005887.

Huang, J.P., Vanacore, E., Niu, F., Levander, A., 2010. Mantle transition zone beneath the Caribbean–South American plate boundary and its tectonic implications. *Earth Planet. Sci. Lett.* 289, 105–111. doi:10.1016/j.epsl.2009.10.033.

Kellogg, J., Bonini, W., 1982. Subduction of the Caribbean plate and basement uplifts in the overriding South American plate. *Tectonics* 1, 251–276.

Li, J., Niu, F., 2010. Seismic anisotropy and mantle flow beneath northeast China inferred from regional seismic networks. *J. Geophys. Res.* 115, B12327. doi:10.1029/2010JB007470.

Mainprice, D., Silver, P.G., 1993. Interpretation of SKS-waves using samples from the subcontinental lithosphere. *Phys. Earth Planet. Inter.* 78, 257–280.

Malave, G., Suarez, G., 1995. Intermediate-depth seismicity in northern Colombia and western Venezuela and its relationship to Caribbean plate subduction. *Tectonics* 14, 617–628.

Miller, M.S., Levander, A., Niu, F., Li, A., 2009. Upper mantle structure beneath the Caribbean–South American plate boundary from surface wave tomography. *J. Geophys. Res.* 114, B01312. doi:10.1029/2007JB005507.

Molnar, P., Sykes, L.R., 1969. Tectonics of the Caribbean and Middle America Regions from focal mechanisms and seismicity. *Geol. Soc. Am. Bull.* 80, 1639.

Niu, F., Li, J., 2011. Component azimuths of the CEArray stations estimated from P-wave particle motion. *Earthquake Sci.* 24, 3–13.

Niu, F., Baldwin, T., Pavlis, G., Vernon, F., Rendon, H., Bezada, M., Levander, A., 2007. Receiver function study of the crustal structure of the Southeastern Caribbean Plate Boundary and Venezuela. *J. Geophys. Res.* 112, B11308. doi:10.1029/2006JB004802.

Pinero-Feliciani, L., Kendall, J., 2008. Sub-slab mantle flow parallel to the Caribbean plate boundaries: inferences from SKS splitting. *Tectonophysics* 462, 22–34. doi:10.1016/j.tecto.2008.01.022.

Russo, R., Silver, P.G., 1994. Trench-parallel flow beneath the Nazca Plate from seismic anisotropy. *Science* 263, 1105–1111.

Russo, R., Silver, P.G., Franke, M., Ambeh, W.B., James, D.E., 1996. Shear-wave splitting in northeast Venezuela, Trinidad, and the eastern Caribbean. *Phys. Earth Planet. Inter.* 95, 251–275. doi:10.1016/0031-9201(95)03128-6.

Savage, M.K., 1999. Seismic anisotropy and mantle deformation: what have we learned from shear wave splitting? *Rev. Geophys.* 37, 65–106.

Schulte-Pelkum, V., Blackman, D.K., 2003. A synthesis of seismic P and S anisotropy. *Geophys. J. Int.* 154 (1), 166–178.

Silver, P.G., 1996. Seismic anisotropy beneath the continents: probing the depths of Geology. *Annu. Rev. Earth Planet. Sci.* 24, 385–432.

Silver, P.G., Chan, W., 1988. Implications for continental structure and evolution from seismic anisotropy. *Nature* 335, 34–39.

Silver, P.G., Chan, W., 1991. Shear-wave splitting and subcontinental mantle deformation. *J. Geophys. Res.* 96 (16), 429–16, 454.

Silver, P.G., Savage, M.K., 1994. The interpretation of shear-wave splitting parameters in the presence of two anisotropic layers. *Geophys. J. Int.* 119, 949–963.

Taboada, A., Rivera, L., Fuenzalida, A., Cisternas, A., Philip, H., Bijwaard, H., Olaya, J., Rivera, C., 2000. Geodynamics of the northern Andes: subductions and intracontinental deformation (Colombia). *Tectonics* 19, 787–813.

Van der Hilst, R., Mann, P., 1994. Tectonic implications of tomographic images of subducted lithosphere beneath northwestern South America. *Geology* 22, 451–454.

Weber, J., Dixon, T., DeMets, C., Amberth, W., Jansma, P., Mattioli, G., Saleh, J., Sella, G., Bilham, R., Perez, O., 2001. GPS estimate of relative motion between the Caribbean and South American plates, and geologic implications for Trinidad and Venezuela. *Geology* 29, 75–78.

Wolfe, C.J., Silver, P.G., 1998. Seismic anisotropy of oceanic upper mantle: shear wave splitting methodologies and observations. *J. Geophys. Res. Solid Earth* 103, 749–771.